International Journal of Heat and Mass Transfer 227 (2024) 125498

Contents lists available at ScienceDirect

International Journal of Heat and Mass Transfer

journal homepage: www.elsevier.com/locate/ijhmt

Drop rebounding on heated micro-textured surfaces

M. Toprak [a,c], N. Samkhaniani [b], A. Stroh [b,*]

[a] TU Darmstadt, Chair of Fluid Dynamics, 64287, Darmstadt, Germany
[b] Karlsruhe Institute of Technology, Institute of Fluid Mechanics, 76131, Karlsruhe, Germany
[c] TU Darmstadt, Graduate School of Computational Engineering, 64293, Darmstadt, Germany

ARTICLE INFO

Keywords:
Superhydrophobic surfaces
Heat transfer
Drop impact
Phase-field method
OpenFOAM
Textured surfaces

ABSTRACT

This study investigates the hydrodynamics and heat transfer of a droplet impinging on a heated superhydrophobic surface at low Weber numbers with subsequent bouncing through numerical simulations in the phase-field framework. These structure-resolved simulations take into consideration the entrapment of air during impingement on the micro-textured surface and effectively replicate the hydrodynamic behavior observed in corresponding experimental studies [1]. The simulation results indicate notable differences in air entrainment and heat transfer dynamics for the same contact angle under varying surface topography. This offers the potential to deliberately modify the dynamics of heat transfer by manipulating the surface topography without significantly altering the wetting behavior. Additionally, an attempt to substitute the structure-resolved boundary with a temperature boundary condition, which incorporates the void fraction and thermal conductivity of the involved fluids, has been observed to be insufficient to reproduce the temperature evolution due to the absence of wetting physics description. These findings suggest that the primary source of variations in heat transfer is the alteration in the contact area with the surface, rather than the local thermophysical properties of the air/water mixture. Consequently, for an accurate evaluation of heat transfer on textured surfaces, it is imperative to employ simulations that consider the resolved surface topography.

1. Introduction

Central to many technological and industrial processes such as spray cooling and fuel injection is the phenomenon of individual droplets impacting on heated surfaces [2]. One of the main goals in such processes is the enhancement of the heat transfer rate between the liquid and the solid surface [3]. Effective heat transfer requires that liquid comes into direct contact with the solid surface upon impact, however, a formation of thick liquid film over a surface is usually not favorable, as it reduces the heat transfer rate from the solid surface. For instance, in selective catalytic reduction (SCR) systems, such film formation due to the injection of a urea-water solution into automotive exhaust gas is considered to be undesirable [4]. This is linked to the fact that the film evaporation produces unwanted intermediates and by-products forming solid deposits [5], which impair the overall system performance. In such a case, the effect can be mitigated by a reduction of the drop contact time with the heated solid surfaces [6]. Analogous strategies are available in various contexts such as spray cooling [7,8], anti-acing [9], coating [10], refrigeration [11], and falling film evaporation [12]. By managing the interaction between liquid and solid surfaces, these approaches aim to optimize their performance and enhance overall effectiveness.

Various parameters such as drop diameter, d_0, drop impact velocity, U_0, gas-liquid surface tension, σ, and physical properties of the droplet (density ρ and viscosity μ) determine the droplet behavior after impact on the flat surface. The outcome of drop impingement can be categorized into deposition, rebounding, and splashing [13]. The outcome is governed by a balance between the inertial, viscous, and surface tension forces. Hereby, the main characteristic non-dimensional number is the Weber number $We = \rho {U_0}^2 d_0/\sigma$ [14], showing the importance of the drop inertia compared to its surface tension. In addition, the Reynolds number $Re = \rho U_0 d_0/\mu$ plays an auxiliary role by characterizing the ratio of inertial to viscous forces. Another influential parameter is the surface wettability, which is mainly determined by the chemical composition and surface properties such as surface roughness and its topography. The hydrodynamic effect of surface wettability can be considered via an appropriate description of the contact angle behavior. Using the equilibrium contact angle θ_e, surfaces in contact with the water droplet are classified into hydrophilic ($\theta_e < 90°$) and hydrophobic ($\theta_e > 90°$)

---

* Corresponding author.
E-mail address: alexander.stroh@kit.edu (A. Stroh).

https://doi.org/10.1016/j.ijheatmasstransfer.2024.125498
Received 14 November 2023; Received in revised form 21 March 2024; Accepted 25 March 2024

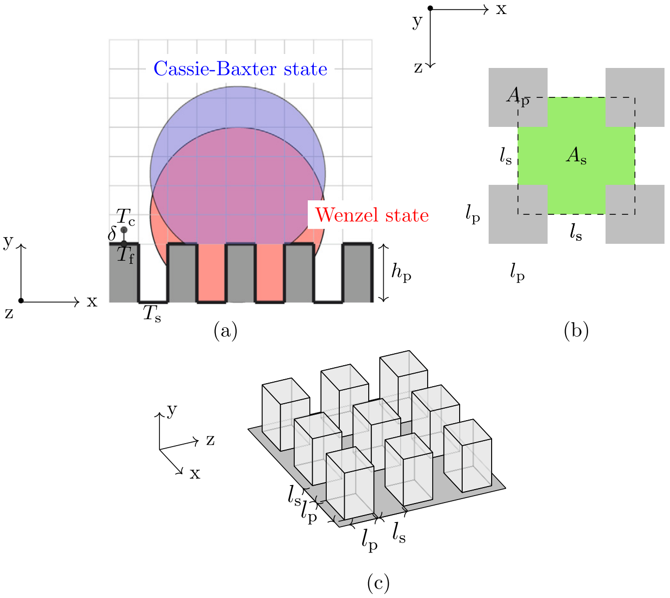

Fig. 1. (a) 2D representation of problem: Cassie-Baxter state (drop is in contact with the surface pins while the valleys are filled with air, blue droplet) or Wenzel state (drop fills the grooves, red droplet), (b) the top view of textured surfaces, (c) illustration of the surface structuring using square prisms. The characteristic dimensions of structured surfaces are: texture height h_p, pin width l_p and gap width l_s. The parameters T_f, T_c, T_s denote the temperatures at cell faces, cell centers and the bottom substrate, respectively. δ is the face-to-cell distance. The green region indicates the void surface A_s among gray solid pillar surfaces A_p. (For interpretation of the colors in the figure(s), the reader is referred to the web version of this article.)

surfaces [15]. The surface topography directly affects the wettability whereas surfaces fabricated with micro/nano-textures can also become superhydrophobic ($\theta_e > 150°$) [16]. As depicted in Fig. 1(a), the embedded micro/nano-texture may form air pockets between the liquid drop and the surface substrate within the roughness troughs, known as Cassie-Baxter state [17]. Depending upon spatial configurations of structures, initial conditions, and thermophysical properties of the liquid drop, the liquid–gas interface may penetrate the troughs between the micro-structures, thereby marking a transition to Wenzel state [18]. The behavior of droplets upon impingement can be altered using various surface structuring techniques. A surface structured with elevated pins can be characterized by the surface area fraction f_v [17], and the surface roughness factor R_p. The surface area fraction is defined as (see Fig. 1,b):

$$f_v = 1.0 - \frac{A_p}{A_s + A_p}, \tag{1}$$

where A_p represents the projected area of the pin region, and A_s represents the projected area of the gap region between the pins. The surface roughness factor represents the ratio of the true apparent surface area to the projected area $A_{app,s}/A_{proj,s}$ and is equal to 1.0 for a smooth surface [19]. For the uniform structured texture surface it is given by:

$$R_p = 1.0 + \frac{4 l_p h_p}{(l_p + l_s)^2}, \tag{2}$$

where l_p and h_p are the sizes of pins and l_s is gap size. The spreading ratio $\beta = d(t)/d_0$, with d_0 representing the initial droplet diameter and $d(t)$, describing the equivalent diameter of wetting area, as well as the film thickness is considered to be the most important characteristics of the droplet impingement hydrodynamics [20,2,14,19,21,22].

In the case of drop impingement on a hot dry solid surface, the impact outcomes are classified into several regimes: evaporation, nucleate boiling, foaming, transitional boiling, and film boiling [23]. Although many studies investigated the droplet impact with high wall temperature conditions in the nucleate boiling and Leidenfrost regime [24,25], only a few have examined wall temperatures lower than the boiling point, i.e., in the film evaporation regime [26]. Roisman [27] pointed out that evaporation is negligible during the spreading and receding stages of bouncing droplets in the film evaporation regime. The outcome of drop impingement at low Weber numbers in the film evaporation regime is thoroughly investigated in our previous studies [28,29]. These studies show that in the rebounding regime, a higher Weber number improves the cooling effectiveness on a smooth surface. Strotos et al. [30,31] proposed an equation for calculating the cooling effectiveness of an impinging droplet on a flat surface using transient heat conduction. However, their model is not intrinsically applicable to textured surfaces. Moon et al. [32] extended the cooling effectiveness model to account for the surface wetting condition after the droplet impact. This modification takes into consideration the wetting behavior of the droplet on the surface. However, in order to use this extended model, experimental data is required to determine the wetting condition of the surface.

The objective of the present study is to understand how a structured textured surface affects heat transfer for a bouncing droplet on film evaporation regime where the substrate temperature is far below saturation temperature and the evaporation is negligible. It is obvious that the surface structuring increases the effective area during the droplet impingement resulting in an enhancement in the heat transfer, however, at the same time, air entrapment in cavities may impair the heat transfer rate compared to a drop impact on a smooth surface. In order to elucidate those scenarios, we consider a resolved simulation of the micro-structure and compare it to an implicit temperature boundary condition mimicking a structured surface with reduced computational cost for the Cassie-Baxter case. A thorough search of the relevant literature yielded that the heat transfer during the impact of a single droplet on a micro-textured hydrophobic surface has not been investigated with resolved simulations before.

2. Methodology

In the present study, the simulation of drop impact at low Weber number on the heated surface is performed with the in-house solver phaseFieldFoam. According to previous studies [27,30,32], the evaporation effect is ignored because the spreading and receding phases took place within a very short time (on the order of ten milliseconds). The computation utilizes the phase-field method with the coupled Cahn-Hilliard-Navier-Stokes equations for two incompressible and immiscible phases being solved using OpenFOAM-extend framework. For more details on governing equations, numerical implementation, and validation of the solver phaseFieldFoam the reader is referred to [28,33].

2.1. Governing equations

In the utilized phase-field method, the order parameter C describes the distribution of liquid (L) and gas (G) phase systems. It takes distinct values of $C = -1$ for liquid and $C = 1$ for gas in the bulk region, while it smoothly varies in the thin transition region at the interface between the phases. The non-dimensional Cahn number $Cn = \varepsilon / L_{ref}$, relates the capillary width ε to the macroscopic characteristic length L_{ref}, which is droplet initial diameter d_0 in the present study and is kept constant at $Cn = 0.01$. Then, the thickness of the diffuse interfacial region 4.16ε is obtained [34]. The diffuse interface transport is specified with the Cahn-Hilliard equation:

$$\frac{\partial C}{\partial t} + \nabla \cdot (\mathbf{u} C) = M \nabla^2 \Phi, \tag{3}$$

where the chemical potential Φ is:

$$\Phi = \frac{\lambda}{\varepsilon^2} C(C^2 - 1) - \lambda \nabla^2 C - \nabla \lambda \cdot \nabla C. \tag{4}$$

The positive diffusion parameter, also referred to as mobility $M = \chi\varepsilon^2$ is proportional to the square of capillary width, while the semi-empirical coefficient χ fixed to $\chi = 1\ \mathrm{m\cdot s\cdot kg^{-1}}$ similar to our previous studies [5,28,29]. The homogeneous mixing energy coefficient is derived for a planar interface at equilibrium as $\lambda = 3\sqrt{2}/4\sigma\varepsilon$ [35]. The Navier-Stokes equation for two incompressible and immiscible phases in one-fluid formulation is given by:

$$\frac{\partial(\rho\mathbf{u})}{\partial t} + \nabla\cdot(\rho\mathbf{u}\mathbf{u}) = -\nabla p_d + \rho\mathbf{g} + \nabla\cdot[\mu(\nabla\mathbf{u} + (\nabla\mathbf{u})^{\mathsf{T}})] + \mathbf{f}_\sigma. \tag{5}$$

The surface tension $\mathbf{f}_\sigma$ is expressed as:

$$\mathbf{f}_\sigma = \Phi\nabla C + \left(\frac{1}{\varepsilon^2}C(C^2-1) + \frac{1}{2}\|\nabla C\|^2\right)\nabla\lambda. \tag{6}$$

We consider constant surface tension without Marangoni effects so the second term on the right-hand side of the equation becomes zero. The energy equation is given by:

$$\frac{\partial T}{\partial t} + \nabla\cdot(\mathbf{u}T) = \nabla\cdot(\alpha\nabla T), \tag{7}$$

where $\alpha = k/\rho c_\mathrm{p}$ is thermal diffusivity. In the interface region, the physical properties $\varphi \in [\mu, k, \rho, c_\mathrm{p}]$ are calculated through arithmetic interpolation $\varphi = \varphi_\mathrm{L}(1+C)/2 + \varphi_\mathrm{G}(1-C)/2$.

2.2. Boundary conditions at the heated wall

For the order parameter, a Neumann boundary condition is obtained accounting for contact angle θ [36]:

$$\mathbf{n}_\mathrm{S}\cdot\nabla C = \frac{\sqrt{2}}{2}\frac{\cos\theta}{\varepsilon}(1-C^2), \tag{8}$$

where $\mathbf{n}_\mathrm{S}$ is the outward unit vector normal to the solid surface. When a drop comes to rest on a smooth, heated surface, its contact angle θ is equal to the equilibrium contact angle θ_e, which is used to characterize the wettability of the surface. In this case, if the substrate temperature T_s is fixed, a Dirichlet boundary condition can be applied to the temperature at the solid boundary face T_f ($T_\mathrm{f} = T_\mathrm{s}$).

Dealing with textured surfaces, two approaches can be employed: the resolved approach and the modeled approach. With the **resolved approach**, all the small features of the textured surface up to the micro-scale are included in the computational grid. The contact angle used for the wall boundary condition remains fixed at θ_e. The temperature at the fluid-solid interface is set equal to the temperature of the solid surface:

$$T_\mathrm{f} = T_\mathrm{s}. \tag{9}$$

With the **modeled approach** we aim to approximate the effect of the texture without explicitly resolving all the geometric details leading to high computational costs. The method employs a 1-dimensional implicit definition for the temperature boundary condition at the solid surface:

$$T_\mathrm{f} = \frac{kT_\mathrm{c}h_\mathrm{p} + k_\mathrm{eff}T_\mathrm{s}\delta}{kh_\mathrm{p} + k_\mathrm{eff}\delta}, \tag{10}$$

where the temperature T_f is determined by estimating the heat flux at the solid-liquid interface, as illustrated in Fig. 1(a). For more complex scenario e.g. superhydrophobic surfaces including temperature jump, the reader is referred to [37]. The influence of air entrapment within the texture's pores is considered by incorporating the effective thermal conductivity, which is given by:

$$k_\mathrm{eff} = f_\mathrm{v}k_\mathrm{G} + (1.0 - f_\mathrm{v})k_\mathrm{S}, \tag{11}$$

where k_G and k_S stand for the thermal conductivity of gas (entrapped air) and solid (silicon) phases, respectively. This boundary condition assumes the establishment of the Cassie-Baxter state, where the apparent contact angle θ_cb is determined as [17]:

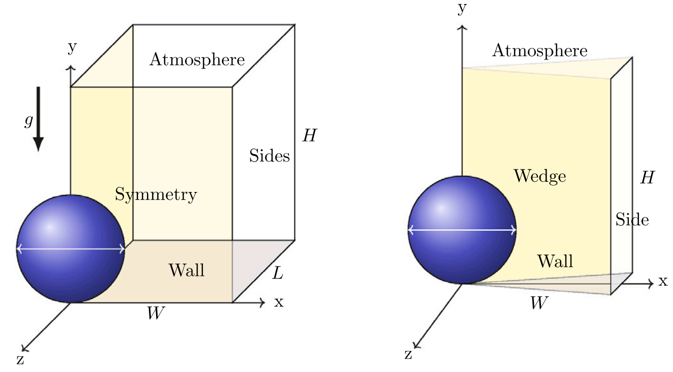

(a) $W \times L \times H = 1.5d_0 \times 2.12d_0 \times 1.5d_0$ (b) $W \times H = 1.5d_0 \times 7.5d_0$

Fig. 2. Schematic representation of the computational setups for drop impact on a solid surface for (a) 3D symmetric and (b) axisymmetric domain.

$$\cos\theta_\mathrm{cb} = -f_\mathrm{v} + (1.0 - f_\mathrm{v})\cos\theta_\mathrm{S}, \tag{12}$$

where θ_S represent the equilibrium contact angles of the drops on the smooth plate. In this case, $\theta = \theta_\mathrm{cb}$ is considered for Eq. (8). More details about the derivation of the temperature implicit boundary condition can be found in Appendix.

3. Validation

This section aims to validate the numerical method implemented in the phasefieldFoam solver for the considered problem setup. Several preceding investigations have already extensively validated the solver in various configurations for the hydrodynamics [22,38–40,5] and for the heat transfer [28]. Here we expand these validation studies with a simulation of the impact of a single droplet on a heated structured hydrophobic surface using two numerical setups corresponding to two available experimental cases. The first case involves comparing the hydrodynamic characteristics of the droplet, such as contact time and spreading behavior on protrusion surfaces, with the experimental results of Jiang et al. [41]. The second case focuses on reproducing the experiment conducted by Guo et al. [1] to study the heat transfer on micro-textured surfaces. Additional two simulations highlighting the resolution effects and the structure feature size are presented in the Appendix.

Fig. 2 provides a visual representation of the computational setups used in both validation cases: 3D domain (a) or axisymmetric quasi 2D domain (b). The choice of the computational domain size is crucial and has been guided by prior investigations to ensure that the results remain independent of the chosen domain size [5,28]. For the present investigation the domain size with $W \times L \times H = 1.5d_0 \times 2.12d_0 \times 1.5d_0$ and $W \times H = 1.5d_0 \times 7.5d_0$ is chosen for 3D and axisymmetric domain, respectively.

For the initial state at $t = 0\,\mathrm{s}$ the droplet center is located at $d_0/2$ above the surface, in contrast to the reference experiments where it has been released from a certain position above the wall. This approach allows to maintain feasible computational costs, although it does not present the same initial condition. The droplet is assumed to be spherical with a diameter of d_0 before impact, and a spatially uniform downward velocity U_0 is prescribed as the initial condition. Due to the point contact of the droplet with the surface, the assessment of a potential thermal boundary layer is excluded, representing a condition whose manifestation in the reference experiments is not documented. Moreover, placing the drop within a potential thermal boundary layer at the initial state would neglect the history of interaction with the surrounding air during its travel towards the wall. Instead, a uniform temperature profile is assigned initially, matching with the droplet temperature specified in the experiments (27.8 °C for $\theta_\mathrm{e} = 140°$ and 27.1 °C for $\theta_\mathrm{e} = 155°$) in diabatic cases. This approach is in line with similar numerical studies [28,42,43].

Table 1
Thermophysical properties.

	μ [Pa.s]	ρ [kg/m^3]	c_p [J/kg K]	k [W/m K]
isothermal cases based on [41]				
Water	1×10^{-3}	1000	-	-
diabatic cases based on [1]				
Water	9.01×10^{-4}	998	4200	0.6
Air	1.48×10^{-5}	1.29	1006	0.026
Silicon	-	2329	700	120

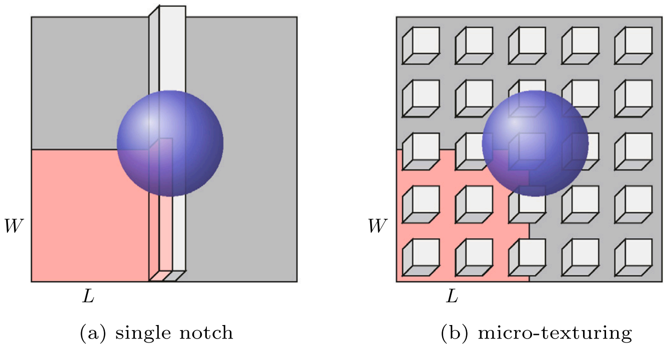

(a) single notch (b) micro-texturing

Fig. 3. Schematic of the structured surfaces. The red area indicates the size of the selected domain for numerical simulation.

At the solid surface, the boundary conditions are set to no-slip for the velocity field in combination with Eq. (8) for the order parameter and Eq. (9) or Eq. (10) for temperature in diabatic cases. It's important to highlight that the no-slip condition only valid for smooth surfaces or simulations employing a resolved approach. In the context of a modeled approach, establishing an accurate velocity boundary condition at the solid surface proves to be intricate and depends on upon the prevailing surface wetting conditions e.g. situations resembling the Cassie-Baxter condition, slip or partially slip conditions might be more suitable, while the no-slip condition, retained for scenarios akin to the Wenzel condition, serves as an approximation [44,45]. At the atmosphere boundary, the totalPressure is used for pressure, while homogeneous Neumann boundary conditions are imposed for velocity and order-parameter. For diabatic cases, the inletOutlet boundary condition is set for temperature. The structured grid is created with the OpenFOAM mesh generator blockMesh utilizing hexahedral cells. The mesh independence is ensured, as the resolution of all the simulations is controlled with Cahn Number $Cn = 0.01$ so the diffuse interface is resolved with 8 cells. The details of thermophysical properties for simulations are summarized in Table 1, the surface tension is set to $\sigma = 0.072$ N/m.

3.1. Isothermal case: drop impact on a single square notch

In the first validation scenario, the simulations are based on the surface topology depicted in Fig. 3a corresponding to the experimental configuration investigated by Jiang et al. [41]. The structure consists of a smooth, flat plate with a single square notch at the top, measuring approximately 1 mm in height. This height is approximately 0.24 times the droplet diameter, which is $d_0 = 4.14$ mm. The equilibrium contact angle for the droplet on this surface is 153.5°. In order to reduce the computational cost, one quarter of the 3D domain with symmetric boundary conditions is employed as depicted in Fig. 2a. The number of cells is given by $N_W \times N_L \times N_H = 150 \times 212 \times 150$. Two cases are examined at $We = 7.1, 20.8$, where the Reynolds numbers are 1450, 2480 with impact velocities of $0.35\,\mathrm{m\,s^{-1}}$ and $0.60\,\mathrm{m\,s^{-1}}$, respectively.

The evolution of the droplet after impact on a single notch is depicted in Fig. 4. Depending on the Weber number, two possible scenarios are observed: rebounding at $We = 7.1$ and breakup of the droplet at $We = 20.8$. The numerical simulation is able to predict all significant characteristics for the considered impact, including the spreading and recoiling process, the formation of capillary waves on the liquid surface, the entrapment of air during impingement, and the generation of satellite droplets following the breakup of the main droplet. The agreement between the numerical simulation and experimental observations demonstrates the capability of the utilized model to accurately capture the essential features of droplet dynamics in this scenario.

For the quantitative comparison, the spreading of the droplets in Fig. 5 is assessed using the droplet's maximum spread-out ratio $\beta^*(t) = d_{\max}(t)/d_0$ where $d_{\max}$ is the maximum projected diameter on planes parallel to the reference plate. Note that with this definition the spread-out ratio starts at $\beta^* = 1$ since in the initial instant $d_{\max} = d_0$. The observed local minimum and maximum values of $\beta^*(t)$ are in good agreement to the experimental data, occurring at almost similar time instants.

A slight difference in the magnitudes between the experimental and numerical curves is observed at later time instances, which can be explained with uncertainty in experimental data and simplifications in numerical setups. The experimental data [41] reports uncertainties of approximately 3% for impact velocity, 10% for Weber number, and 2% for drop flow rate. The empirical correlation of $\beta^*_{\max} \sim We^{0.35}$ is proposed for drop impact on protrusion surfaces [41] which contribute to an uncertainty of at least $e_{\beta^*_{\max}} \sim 3.5\%$ for $\beta^*_{\max}$ calculation in the experiment. It is crucial to note that the uncertainty of $\beta^*_{\max}$ derived from experimental cloud data can potentially be higher than the uncertainty calculation via correlation. It can be up to $10 - 15\%$, as indicated by Fink [22], attributed to nanometric defects on plate surfaces and possible contact line pinning, so deviation up to 15% can be considered as a reasonable agreement.

At $We = 7.1$ the initial spreading ratio is greater than 1, indicating a slightly oblate shape droplet prior to impact, while the numerical simulation assumes a perfect spherical shape. The spreading-out ratio quickly aligns with the experiment as the droplet spreads on the surface before detachment. At the maximum spreading stage (Fig. 4a, b, $t \approx 24$ ms), the droplet appears to spread less in the simulation compared to the experiment, resulting a difference of approximately 14% at the peaks. Then, the drop both in the experiment and simulation demonstrates a sudden contract in the recoiling stage, with the droplet forming bell shape.

For $We = 20.8$ the provided data in the figure only covers the period of time prior to droplet breakup, similar to the reference experiment. The droplet maximum β^* is observed at the breakup instant with a maximum deviation of 9% for $\beta^*_{\max}$. Comparing the final snapshots of the droplets in Fig. 4c and d, it is evident that the drop breakup displays a subtle asymmetry in experiments arises from the aforementioned irregularities in actual experiments and the slight variations in the initial drop shape. However in the simulation due to perfectly symmetrical initial condition, and ideal smooth surface and the imposition of symmetry boundary conditions exhibits a symmetry breakup.

3.2. Diabatic case: drop impact on heated micro-texture surface

In the second validation scenario based on the experiment by Guo et al. [1], a drop impact on micro-textured surface with the void fraction $f_v = 0.56$ is simulated on a smooth surface. The contact angle on the solid plate is $\theta_S = 120°$ and the droplet angle in contact with air is $\theta_G = 180°$. Then, the contact angle based on Cassie-Baxter Eq. (12) becomes $\theta_{cb} = 140°$ and imposed as the equilibrium contact angle θ_e. For this validation, the computational domain is considered axisymmetric, as illustrated in Fig. 2b, and consists of a grid with 150×750 uniformly sized cells.

In Fig. 6, the numerical simulation of drop impact ($d_0 = 2.3$ mm, $We = 20$) on a heated surface ($T_s = 60\,°\mathrm{C}$) is compared with the experiment [1]. The droplet sequence from numerical studies accurately captures the important details of drop hydrodynamics, including the capillary wave ($t = 1.6$ ms), maximum spreading ($t = 3$ ms), and con-

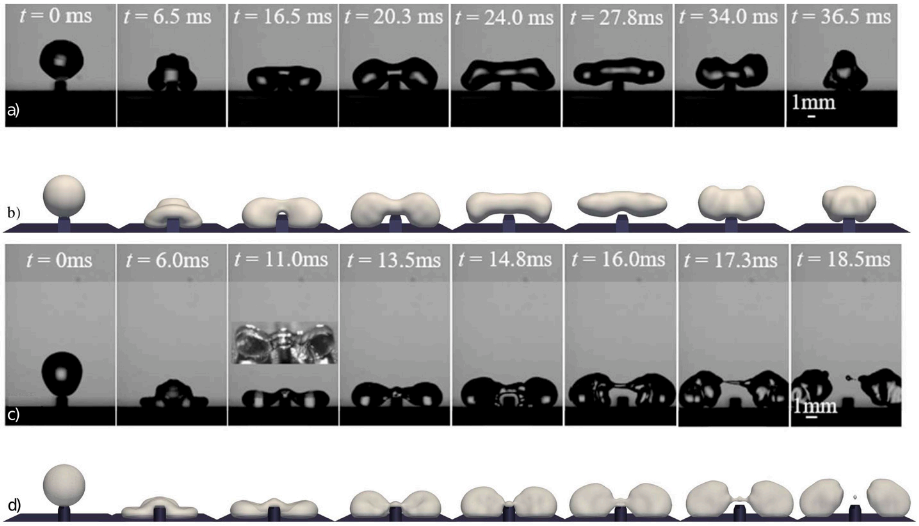

Fig. 4. Comparison of instantaneous droplet shapes for numerical simulation and experiments [41] of a droplet impact on a single notch at Weber number of 7.1 (a, b) and 20.8 (c, d).

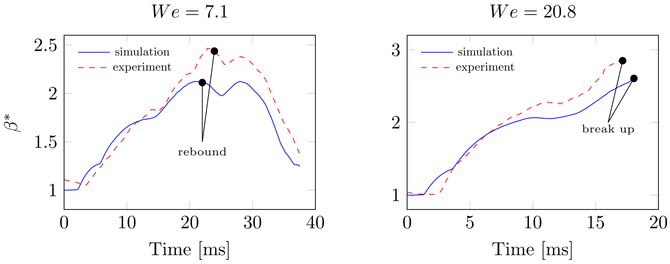

Fig. 5. Time history of maximum spread-out ratio compared with the experiment [41] for droplet impact on the square notch. The simulations are performed on a 3D symmetric domain with a notch.

tact time. Fig. 7 shows a comparison of temperature contours between the numerical simulation and high-speed infrared (IR) thermography data from [1]. The temperature contours exhibit a fair similarity. However, it should be noted that the informational content of IR images may be limited due to the presence of motion blur and high temperature bands at the droplet interface, which is linked to the fact that the droplet temperature, according to the authors, is captured with a hot surface at 60 °C placed in an environment with a background temperature of 50 °C. To mitigate these artifacts, the experimental droplet mean temperature is approximated by considering only the central part of the droplet surface, taking into account only the inner 20% of the pixels away from the surfaces (for more details the reader is referred to the original publication [1]). The numerical simulation calculates the mean temperature based on the entire droplet volume (Ω) using

$$T_\mathrm{d} = \frac{\int_\Omega T \,\mathrm{d}V}{\int_\Omega \mathrm{d}V}, \tag{13}$$

or the mean surface temperature integrated within the volume of diffuse interface Ω_s $(-0.75 > C > 0.75)$:

$$T_\mathrm{surf} = \frac{\int_{\Omega_s} T \,\mathrm{d}V}{\int_{\Omega_s} \mathrm{d}V}. \tag{14}$$

Further evaluation techniques trying to mimick experimental post-processing pipeline have been tested, but essentially delivered results similar to T_surf. More information on that can be found in the Appendix. In Fig. 8, the temperature of the droplet is plotted from the first impingement and rebounding to the second impact. The surface-temperature-based estimation is found to be underestimating the drop temperature by 2-3 °C compared to the experimental values of T_d during the detached phase and overestimating it during the impingement. The volume-based temperature T_d from simulation in turn shows a good agreement with the experimental results at the time before the impact or during the spreading phase, when the drop temperature distribution is almost uniform. The maximum volume-averaged temperature is observed after maximum spreading in the recoil stage is reached. Herein, the computed droplet temperature strongly deviates from the experiment. This might be related to the fact that the temperature distribution in the drop is highly non-uniform in the liquid film near the heated plate and, in the experiment, the region near the droplet bottom is excluded from the estimation of mean temperature as indicated in Fig. 7. Hence, a portion of temperature information near the heated solid is missing. The difference between experimental T_d and numerical T_surf might be associated with the effects of local variation in emissivity and reflectivity due to the incident angle of the interface [46], which is not considered for the evaluation of temperature distribution in the experimental reference. Additionally, the transmission of the thermal radiation within the droplet might also affect the captured infrared thermography distributions providing information on temperature distribution also within a certain peripheral layer at the droplet interface [47]. Furthermore, the gray zone in Fig. 8 represents the time period where some parts of the droplet are located outside of the experimental observation frame. To our understanding, this leads to the presence of strong variation of T_d observed in the experimental profile. It has to be noted that both simulation drop temperatures coincide with the experimental values at the time instants around t =75-80 ms, which is in line with the experiment-based observation that the captured droplet temperature is supposed to represent the bulk temperature just prior to the second impingement event.

In order to examine the effect of air entrapment on heat transfer rate, both Eq. (9) applied to the resolved structure simulation and Eq. (10) applied as a modeled temperature boundary condition on the wall are tested. Fig. 9 depicts the comparison of the two considered thermal boundary conditions at the heated wall for the corresponding simulations until the rebound. The modeled temperature represents the dynamic temperature that accounts for the air entrapment. As can be seen, it induces only a marginal reduction in the resultant surface temperature and the surface temperature (T_s) at the bottom overlaps with the fixed boundary condition toward the detachment. Accordingly, it is observed that application of the Dirichlet boundary condition to the resolved structure instead of the modeled temperature does not affect the droplet mean temperature. Another drawback is that the model does not account for the possible increase in the effective contact area since

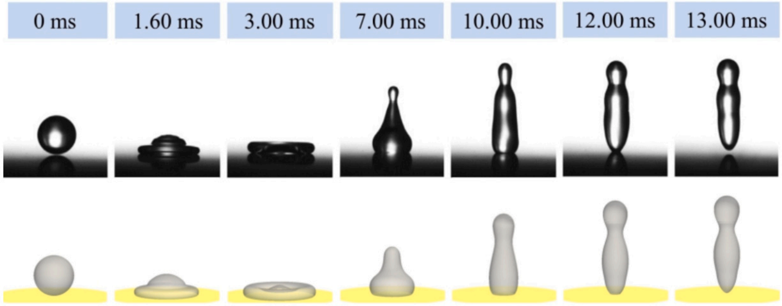

Fig. 6. Image sequence of a bouncing droplet with $d_0 = 2.3$ mm, $We = 20$. Top: experiment [1], bottom: smooth axis-symmetric simulation with $\theta_e = 140°$, adopted from [28].

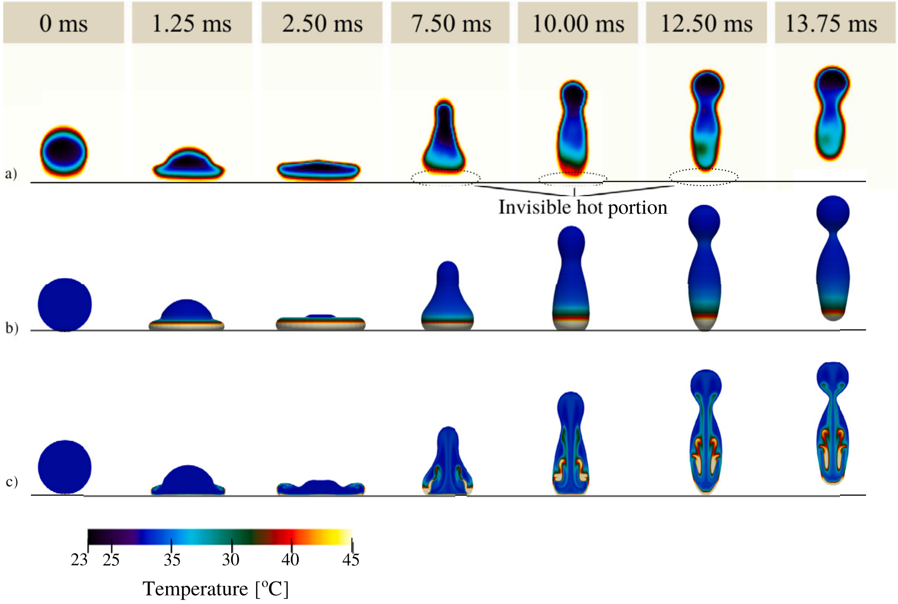

Fig. 7. Temperature contours for the droplet with $d_0 = 2.3$ mm, $We = 20$, $T_{d,0} = 27.8$ °C, and $T_s = 60$ °C: a) high-speed infrared imaging [1], b) droplet interface and c) internal temperature of the smooth axisymmetric simulation with $\theta_e = 140°$. Simulation figures use the same color bar as in the reference experiment.

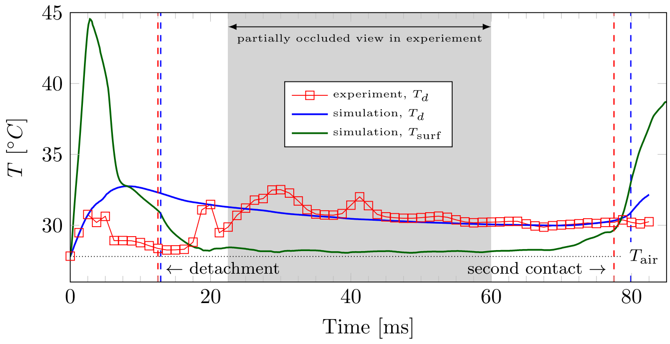

Fig. 8. Comparison of the drop temperature between experiment [1] and axisymmetric simulation of droplet impact on smooth surface with $d_0 = 2.3$ mm, $We = 20$, $T_{d,0} = 27.8$ °C, and $T_s = 60$ °C.

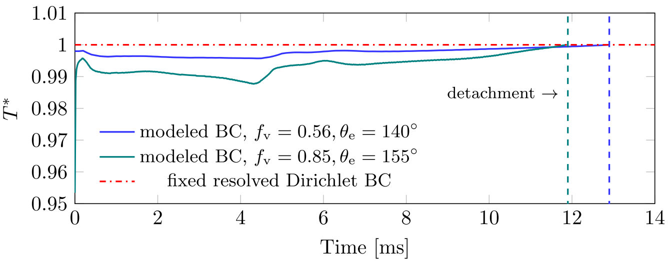

Fig. 9. Dimensionless average surface temperature $T^* = (T_f - T_{d,0})/(T_{s,0} - T_{d,0})$ for the fixed surface temperature in resolved structure scenario (Eq. (9)) and the modeled temperature boundary condition (Eq. (10)).

it is based on the assumption of a full Cassie-Baxter condition. To accurately account for surface conditions, the surface structure has to be resolved.

4. Result and discussion

In order to understand how surface structure affects the droplet behavior, a series of drop impingement with $We = 20$ and $d_0 = 2.3$ mm are simulated under varying surface structure topography. The solid contact angle $\theta_S = 120°$ and the overall surface area fraction $f_v = 0.85$ is the same for all considered textured surfaces. Thus, the equilibrium contact angle is 120° on a smooth surface, which increases up to 155° due to air entrapment in the Cassie-Baxter condition.

In this series of simulation, the resolved approach is employed. A quarter of the 3D computational domain as illustrated in Fig. 2a is utilized with $W \times L \times H = d_0 \times d_0 \times 3d_0$ and discretized with a grid resolution of $200 \times 200 \times 600$ hexahedral cells. A structured region with $[d_0 \times d_0 \times h_p]$ as depicted in Fig. 3b, is created by repeating prisms with dimensions of $[l_p \times l_p \times h_p]$ as demonstrated in Fig. 1c and added to the bottom by using the same grid resolution. The height of the square pin pillars is fixed to $h_p = 80$ μm while the pillar width l_p is varied to

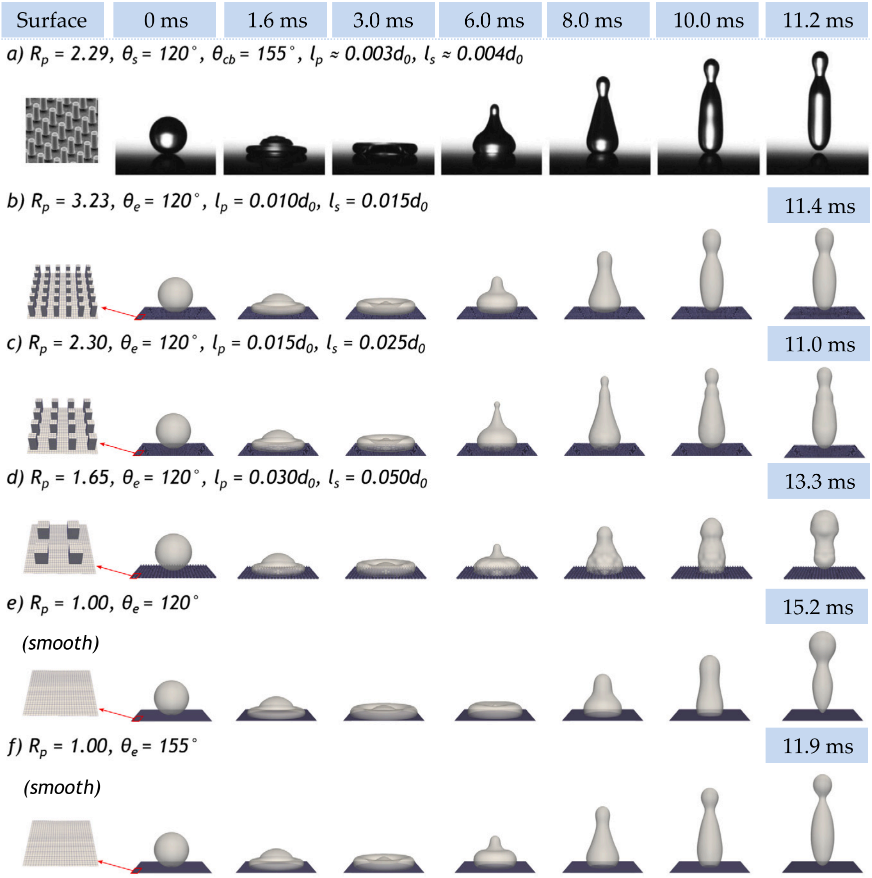

Fig. 10. The comparison of experimental images [1] (a) at $d_0 = 2.3$ mm and $We = 20$ with instantaneous droplet shapes for the 3D textured surface simulations (b, c, d) and for the 3D smooth surface simulations (e, f) with two different contact angles. The last column shows the drop instant at rebound corresponds to the contact time.

create different substrates, so $l_p = 23, 34.5, 69.0$ μm. The corresponding gap sizes and roughness factors are determined as $l_s = 34.5, 57.5, 115$ μm, and $R_p = 3.23, 2.30, 1.65$ respectively. The roughness factor of the experimental surface is calculated as 2.29. The resulting meshes consist of approximately 24.3 million cells with the uniformly distributed cell size of $\Delta x = 0.005d_0$, corresponding to a physical length of 11.5 μm. The number of cells in the smallest single gap among pillars varies from 42 to 420 cells depending on the square pin size. Mass conservation in these simulations has been verified by monitoring the time history of the droplet volume. The deviation in volume remains below 0.0001% of the initial droplet volume throughout the entire simulation period.

Two smooth surface configurations are simulated as reference cases: one with an equilibrium contact angle θ_e equal to θ_S (i.e., $\theta_e = \theta_S$ = 120°) and another with $\theta_e = \theta_{cb}$ = 155° to investigate the effect of surface topography on drop behavior mimicked through variation in contact angle. The simulations aim to explore how the surface properties can be accounted for using the Cassie-Baxter condition described by Eq. (12).

4.1. Contact time

In Fig. 10 the visual comparison of drop impingement on different micro-structured surface is presented. The last picture in each line corresponds to the contact time at which the rebound stage begins. The experiment conducted by Guo et al. [1] investigates a textured surface with roughness and void fraction comparable to our numerical simulation. However, there are some differences in the pin and gap sizes used in the experiment. Specifically, the pin size in the experiment is $l_p = 7$ μm, while the gap size is $l_s = 9$ μm. It is also worth noting that the pins in the experiment are cylindrical in shape, which contrasts with the square-shaped pins used in our numerical simulation.

In the simulation of a smooth surface using both contact angles (120° and 155°), the contact time is overestimated compared to the experimental results. However, the visual comparison shows better agreement with the experiment for the contact angle of 155° as reported by Guo et al. [1], confirming the Cassie-Baxter condition. During the spreading stage, which is governed by inertia, the drop behavior is nearly the same on both smooth and textured surfaces (for $t \lesssim 3$ ms). The main difference arises during the recoiling stage, where friction forces play a significant role. The shear force between a water droplet and a solid plate is much higher than the force between a droplet and a gas layer. Consequently, the contact time for smooth cases is longer due to the absence of drop interaction with gas layer. For textured surfaces, the behavior is more complex. On one hand, the contact area varies based on the structure topography and the wetted area may become larger than in the smooth case if the Wenzel state occurs and the droplet wets the sides of pillar substrates. In this case, the contact time period will tend to be much longer. On the other hand, if the Cassie-Baxter condition applies, a smaller portion of the droplet stays in contact with the solid surface, while the rest is in contact with air, resulting in lower friction and a smaller contact time.

In general in the same void fraction, higher roughness factors resulting from smaller pillar separations lead to reduced contact time as the drop can not fully penetrate into the surface texture and the chance of air entrapment increases which leads smaller shear stress in recoil stage. This is why the textured surface simulation with $R_p = 1.65$ exhibits a significantly longer contact time compared to other compact textured surfaces, indicating that this particular textured surface aligns more with the Wenzel condition rather than the Cassie-Baxter condi-

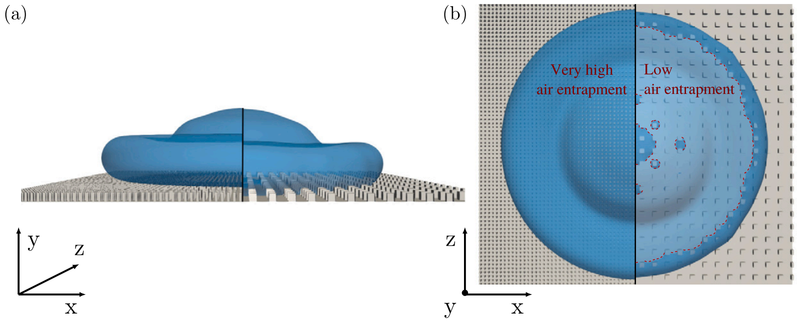

Fig. 11. Side (a) and top (b) views of instantaneous droplet shapes of the 3D textured simulations with $R_\mathrm{p} = 3.23$ (left) and $R_\mathrm{p} = 1.65$ (right) at $t = 2$ ms. The red lines mark the three-phase-contact line.

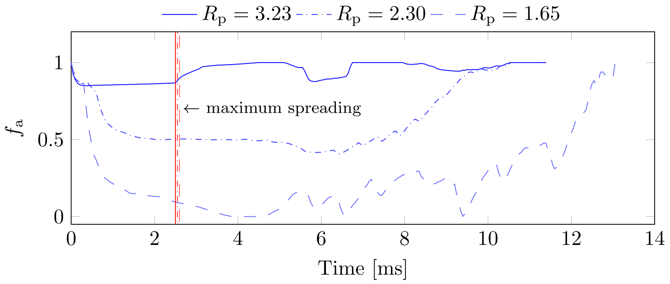

Fig. 12. Time history of air entrapment f_a for the 3D drop impact simulations with surface fraction $f_\mathrm{v} = 0.85$ various micro-textured surfaces. The data are demonstrated until the rebound for each case.

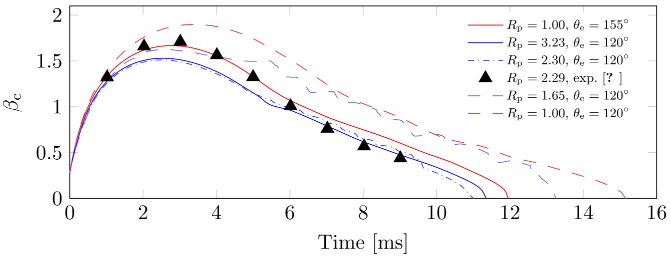

Fig. 13. The spreading ratio of droplet ($d_0 = 2.3$ mm, $We = 20$) on different textured ($R_\mathrm{p} > 1.00$) and smooth ($R_\mathrm{p} = 1.00$) surfaces.

tion. Interestingly, the case with $R_\mathrm{p} = 2.30$ demonstrates the shortest contact time, breaking the trend of decreasing contact time with increasing structure size in the textured surfaces. This behavior can be attributed to the droplet shape and the presence of capillary waves as can be seen in Fig. 10. During the recoiling stage (for around $t > 3$ ms), the central part of the droplet quickly rises up and creates an elongated shape, which combined with the capillary waves results in lower contact time.

4.2. Air entrapment

Fig. 11 provides an example of air entrapment beneath the droplet during impingement on the textured surface. The presence of texture leads to different degrees of air entrapment during droplet impingement. The parameter f_a is introduced to characterizing air entrapment between the pillars. It is quantified as $f_\mathrm{a} = 1.0 - A_\mathrm{bot,c}/A_\mathrm{top,c}$ and represents the difference between the droplet contact areas at the pillars root ($h = 0$) to pillars tip ($h = h_\mathrm{p}$). In essence, when $f_\mathrm{a} = 0$, the substrate is totally wetted, indicating the Wenzel condition. When $f_\mathrm{a} = 1.0$, the droplet only contacts the pillars' tips, leading to a non-wetting Cassie-Baxter condition. A value between 0 and 1 represents a transition between Wenzel and Cassie conditions.

The temporal air entrapment index during drop impingement is presented in Fig. 12 for different textured surfaces. Please note, that air entrapment does not occur on smooth surfaces. The size of the gaps between the micro-pillars of the surface texture, represented by the roughness factor R_p strongly influences the air entrapment underneath the droplet. The case with $R_\mathrm{p} = 3.23$ with compact pillar arrangement exhibits the highest level of air entrapment, reaching the Cassie-Baxter state or non-wetting condition. In this case, a significant portion of the droplet surface remains suspended on the air pockets entrapped in the textured surface. Only slight portion of droplet exhibits wetting along the pillar without reaching the substrate of the textured surface during the spreading stage. Conversely, the case with pillar dispersed arrangement at $R_\mathrm{p} = 1.65$ with $l_\mathrm{s} = 0.05 d_0$ experiences almost no air entrapment or total-wetting condition, approaching the Wenzel state. In this scenario, some small bubbles of entrapped air can be observed adhering to the surface substrate at the drop impact point. The surface at $R_\mathrm{p} = 2.30$ exhibits a partial-wetting condition where neither a full penetration nor a high air entrapment occurs. It falls somewhere between those extremes with $f_\mathrm{a} \approx 0.5$ during both droplet spreading and recoiling stage. In this scenario, various segments of the droplet showcase distinct wetting behaviors: some portions adhere to and wet the substrates, others wet the pillars, while yet another part of the droplet merely touches the tips of the pillars. The evaluation of Laplace pressure i.e. pressure drop across the liquid-gas interface during the initial state of impingement shows that higher Laplace pressure can be observed within the gaps of surface texture for higher roughness factors – around 400, 700 and 1000 Pa for $R_p = 1.65$, 2.30 & 3.23, correspondingly. The higher pressure drop is known to increase repellency of a microstructured surface, so the observed trends are in line with the literature reports [48]. The temporal dynamics of wetting conditions are visually depicted through the incorporation of additional videos which are made available in the supplementary material.

This section reveals for drop impingement at identical Weber number on the surfaces with the same void fraction textured, the surface topology plays a crucial role on the wetting condition. Introducing variations in the Weber number further underscores the complexity of the wetting phenomenon. So the simplified models such as Eq. (12) and Eq. (11) based only on the surface void fraction are insufficient to account the whole air entrapment phenomena. This is evident from the absence of air entrapment in cases with lower R_p values compared to both the experimental and high R_p simulation results at Fig. 13 in the next section. Higher surface roughness factor indicates the presence of compact pillar arrangement with slimmer gaps, resulting in a smaller l_s/d_0 ratio, which promotes air entrapment under droplets during impact.

4.3. Spreading ratio

The spreading behavior of a drop impingement is quantified with the spreading ratio $\beta_\mathrm{c} = d_\mathrm{c}(t)/d_0$ on the contact plane with respect to the experiment [1]. To estimate the spreading ratio, a reference plane for the contact diameter d_c is introduced in the numerical simulation.

The location of the reference plane is considered as half the interface thickness above the tips of the textured surfaces corresponding to $h_c = 2.08\,d_0\,Cn = 470\,\mu\mathrm{m}$ in order to be able to capture the variation in the order parameter C. In Fig. 13, the estimated spreading ratio from simulations is compared with the experimental data by Guo et al. [1]. The maximum spreading occurs at the smooth surface and $\theta_e = 120°$. Increasing the contact angle up to 155° decreases both β_c and contact time as the surface becomes more hydrophobic. Increasing surface roughness hinders drop motion in the spreading stage, while in the recoiling stage, the air entrapment promotes drop rebounding. The textured surfaces with small pin separations ($R_p = 2.30, 3.23$) demonstrate a good agreement with the experiment in the recoiling stage. It can be inferred that both surfaces with high roughness factors and the smooth surface with a contact angle of $\theta_e = 155°$ meet the Cassie-Baxter conditions and are more likely to resemble the experimental observations. At the same time, the rough surface with largest scales at $R_p = 1.65$ and the smooth surface with $\theta_e = 120°$ rather resemble the Wenzel state and significantly deviate from the experimental results. It is worth noting that droplets impinging on textured surfaces with larger pin spacing ($R_p = 1.65$ and $R_p = 2.30$) show step-like behavior in β_c profiles during the recoiling phase, which are not observed for the other textured surface. These steps can be attributed to the dynamic motion of the contact line as it follows the sides of surface features. During this process, the contact line not only conforms to the texture in the wall-parallel plane but also adjusts to its geometry in the wall-normal direction, creating the observed steps in the β_c profiles.

4.4. Energy analysis

Three energy contributions are quantified for the impinging process based on simulation results:

$$\text{surface energy} \quad E_s = \sigma A_{LG} + (\sigma_{LS} - \sigma_{SG}) A_{LS}, \tag{15}$$

$$\text{kinetic energy} \quad E_k = \int_\Omega \rho(\mathbf{u}\cdot\mathbf{u})\,dV, \tag{16}$$

$$\text{gravitational energy} \quad E_g = \int_\Omega \rho|\mathbf{g}|h\,dV, \tag{17}$$

where A_{LG} represents the interface area between liquid and gas, while A_{LS} represents the interface area between liquid and solid. The parameters $\sigma, \sigma_{LS}, \sigma_{SG}$ denote interfacial tensions of the liquid-gas, liquid-solid and solid-gas phases, respectively. The vertical distance, denoted by h, is measured from the bottom wall in the smooth surfaces and from the top of the pins in the textured cases. The total initial energy at $t = 0$ s is obtained as:

$$E_{tot,0} = E_{s,0} + E_{k,0} + E_{g,0} = \sigma\pi d_0^2 + \frac{1}{2}\rho U_0^2 \left(\frac{1}{6}\pi d_0^3\right) + \rho|\mathbf{g}|\frac{d_0}{2}\left(\frac{1}{6}\pi d_0^3\right). \tag{18}$$

The energy dissipation during drop impingement can be evaluated using the principle of energy conservation, expressed as $E_d(t) = E_{tot,0} - E_s(t) - E_k(t) - E_g(t)$. It is important to note that the computed energy dissipation represents the viscous dissipation, excluding the energy losses associated with heat transfer. Thus, it solely accounts for mechanical work. Fig. 14 illustrates the energy components of a droplet during drop impingement from impact to the first rebound. It can be observed that the variation in gravitational energy is insignificant compared to the other energy components. The minimum kinetic energy is reached around the maximum spreading ratio, indicating the initiation of the recoiling stage. At this point, the surface energy is at its maximum. Toward the rebound, kinetic energy first reaches a local maximum and then gradually decreases, converting to gravitational and surface energy. Throughout the droplet impingement process, the energy dissipation continuously increases. These qualitative trends remain for all considered configurations, with slight deviations in the contribution magnitudes.

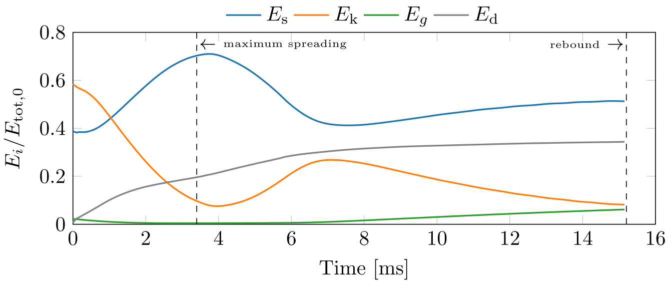

Fig. 14. Variations in energy contributions for the 3D drop impact simulation with $d_0 = 2.3$ mm, $We = 20$ on the smooth surface with $\theta_e = 120°$ for surface (E_s), kinetic (E_k), gravitational (E_g) energies and dissipation (E_d).

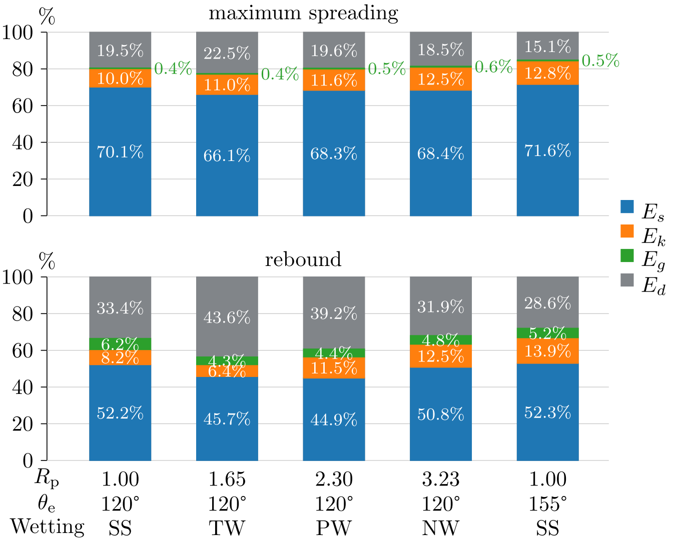

Fig. 15. Instantaneous energy budgets ($E_i/E_{tot,0}$) of the droplets at maximum spreading (top) and detachment point (bottom) for the resolved textured ($R_p > 1.00$) and smooth surface simulations ($R_p = 1.00$). SS: smooth surface, NW: non-wetting, PW: partial-wetting, TW: total-wetting.

Fig. 15 illustrates a comparative analysis of the energy budget at different textured surfaces at $\theta_e = 120°$ in contrast to two smooth surfaces at $\theta_e = 120°, 150°$ during two distinct stages—maximum spreading and rebound—under varying wetting conditions. The graph highlights several important findings: Surface energy (E_s) is lowest on NW surfaces and highest on TW surfaces, indicating variations in droplet wetting and adhesion. NW and PW surfaces show the highest kinetic energy (E_k) during both maximum spreading and rebound, reflecting air entrapment preserves drop kinetic energy as reduces energy dissipation due to viscous effect. In contrast, TW surfaces exhibit the highest dissipated energy (E_d), signifying greater energy loss due to viscous effects and contact line pinning.

4.5. Heat transfer

The cooling effectiveness γ is a measure of how well a droplet absorbs heat compared to the maximum amount of heat it could potentially absorb [1]. It is defined as:

$$\gamma(t) = \frac{m\,c_v\,(T_d(t) - T_{d,0})}{m\,c_v\,(T_s - T_{d,0})}, \tag{19}$$

where m is the mass of the droplet, c_v is the specific heat capacity and T_d and T_s are the temperatures of the droplet and the substrate temperature, respectively. This approach considers the total heat transfer

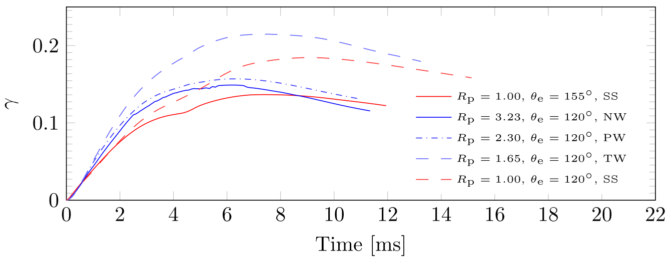

Fig. 16. Bulk cooling effectiveness values of the 3D resolved simulations with $d_0 = 2.3\,\text{mm}$, $We = 20$. SS: Smooth surface, NW: Non-wetting, PW: Partial-wetting, TW: Total-wetting.

by the droplet including the convective heat transfer from the thermal boundary layer.

The temporal evolution of cooling effectiveness is depicted in Fig. 16. After impingement, the average temperature of the droplet experiences a rapid increase. This temperature rise can be attributed to the significant temperature gradient existing between the thin liquid film during the spreading stage and the heated solid substrate. The heat transfer from the solid surface to the droplet leads to a rapid increase in droplet temperature indicating the wall heat transfer is the strongest during the spreading phase confirming the observations by Herbert et al. [49]. Subsequently, during the recoiling stage ($t > 3$ ms), the rate of cooling effectiveness gradually decreases. This phenomenon mainly arises due to the reduction in the contact area between the droplet and the solid substrate. As the droplet recoils, the contact area diminishes, and the upper portion of the droplet becomes surrounded by the bulk air at a lower temperature. Consequently, the heat transfer is mitigated, resulting in a gradual decline in the cooling effectiveness.

The parameters that influence the overall cooling effectiveness in the first place are the contact area, the air entrapment index, and the contact time. No distinct trend between R_p and final γ values can be observed as the simulations yield different air entrapment values altering droplet hydrodynamics. During the spreading stage, all textured surfaces exhibit improved heat transfer into the droplet compared to smooth surface simulations, as a result of their increased surface area, which is characterized by the roughness factor R_p. Then, the cooling effectiveness substantially depends on the wetting state. For the present study, the total heat transfer to the droplet is smaller in a non-wetting case ($R_p = 3.23$) or a partially-wetting case ($R_p = 2.30$) than in flat surfaces but for total-wetting conditions ($R_p = 1.65$), it is vice versa. These results display the influence of contact area and are compatible with previous studies [32,50,51].

In Figs. 10 and 13, it is evident that the textured cases with $R_p = 2.30$ and $R_p = 3.23$ exhibit similar spreading behavior, indicating comparable droplet hydrodynamics. Despite the slightly shorter contact time for the case with $R_p = 2.30$, it results in a distinct enhancement in heat transfer, with a 13% increase in the final γ value compared to the case with $R_p = 3.23$. The primary factor contributing to this difference is the increased contact area beneath the droplet in contact with the heated surface texture. The textured surface with $R_p = 2.30$ provides a larger contact area, enabling more efficient heat transfer compared to the case with $R_p = 3.23$. These findings suggest that surface topology plays a significant role in achieving notable variations in bulk cooling effectiveness, thereby holding substantial potential for relevant engineering applications. For instance, the strategic introduction of larger gap sizes on a surface, which slightly reduces R_p while maintaining the same void ratio, can enhance overall system efficiency in heat transfer without compromising droplet spreading characteristics.

Among all the simulated cases, the textured case with the lowest roughness (i.e. $R_p = 1.65$) demonstrates the highest final cooling effectiveness with $\gamma \approx 0.18$. As discussed in the previous sections, this particular case does not reproduce the superhydrophobic wetting characteristics observed in the experiment or other simulations. Instead, it experiences a full penetration into the pins during the drop impact (total-wetting) as shown in Fig. 11 and spreads more compared to the other textured surfaces as shown in Fig. 13. Nevertheless, this design might be advantageous in certain engineering applications, as it facilitates increased contact area without air entrainment. Consequently, it achieves the highest cooling effectiveness among the textured and smooth cases with the same material properties (i.e. $\theta_e = 120°$).

5. Conclusion

The present numerical study is shown to be able to reproduce experimental observations of a drop impact on smooth and structured surface and can be considered as a complementary tool for extraction of further details on impinging process. In this work, we firstly observe that a consideration of the structured surface through the so-called **modeled approach** utilizing a corrected boundary condition for the temperature instead of resolving the structure does not deliver meaningful results, since this simplification cannot capture the effect of the contact area change. Hence, for a better understanding of the influence of micro-texture topography during drop impingement, a series of numerical simulations with the **resolved approach** is conducted.

It is confirmed that the wetting characteristics of superhydrophobic textured surfaces can be replicated using the phase-field method. This is achieved by mimicking the surface topography with the same void ratio as the substrate in the reference experimental study utilizing a square-shaped pin for texture. Surface topography, characterized by the roughness factor R_p, is found to strongly influence the air entrainment behavior during droplet impingement. Higher roughness factor values lead to increased air entrainment and a greater resemblance to the Cassie-Baxter state. The effect of surface structuring on air entrapment cannot be fully linked to the void ratio alone, as there is a positive correlation between surface roughness and air entrapment. The surface roughness and the size of gaps between considered micro-pillars play a crucial role in the intensification of air entrapment under droplets. Based on our simulation results, we observe that the cooling effectiveness of drop impingement on a heated wall can be altered by manipulating the surface topology. Textured surfaces with low roughness factor values enhance the heat exchange with the wall surface compared to smooth surface simulations, as the contact area increases. Conversely, the textured surfaces with high roughness factor values can lead to a more intricate behavior, potentially resulting in both enhanced and reduced cooling effectiveness depending on their impact on wetting. Additional investigations incorporating a systematic examination of diverse surface topographies, pin heights, droplet sizes, Weber numbers, and wall temperatures have the potential to uncover more insights into the phenomenon of drop impingement on structured surfaces, thereby enhancing our understanding of this subject.

CRediT authorship contribution statement

M. Toprak: Writing – review & editing, Writing – original draft, Visualization, Validation, Software, Methodology, Investigation, Formal analysis, Data curation. **N. Samkhaniani:** Writing – review & editing, Writing – original draft, Supervision, Project administration, Methodology, Investigation, Formal analysis, Conceptualization. **A. Stroh:** Writing – review & editing, Writing – original draft, Visualization, Validation, Supervision, Project administration, Funding acquisition, Data curation, Conceptualization.

Declaration of competing interest

The authors declare that they have no known competing financial interests or personal relationships that could have appeared to influence the work reported in this paper.

Data availability

Data will be made available on request.

Acknowledgements

We express our gratitude to Chunfang Guo for generously supplying supplementary experimental data, and to Dr. Martin Wörner for engaging in insightful discussions. We gratefully acknowledge the financial support by the German Research Foundation (DFG) through the Research Unit 2383 ProMiSe under Grant No. 274353615. In addition, the authors acknowledge support by the state of Baden–Württemberg through bwHPC.

Appendix

Modeled temperature boundary condition

The dynamic boundary condition to implicitly treat the air entrainment beneath the droplets is calculated by a conductive heat transfer equilibrium achieved at the top of pins on the surface, between the neighbor cell center and the bottom of the pins. The variation of the temperature and velocity profiles beneath the pins is neglected. The effective conductivity k_{eff} combining the pins and entrapped air is calculated with respect to Eq. (11).

The total heat transfer Q is calculated by the multiplication of contact area A_{c} and heat flux $\mathbf{q}$ and semi-discretized in 1-dimension as:

$$\frac{\partial Q}{\partial t} = A_{\mathrm{c}}\, k \frac{\Delta T}{H}, \tag{20}$$

where k is the thermal conductivity, ΔT is the temperature difference and H is the vertical distance from the boundary face.

The thermal conductivity of a cell is calculated by the weighted arithmetic interpolation of thermal properties of fluids with respect to order parameter C, and denoted by k. The temperature at cell centers and faces is denoted by T_{c} and T_{f}, while the substrate temperature is denoted by T_{s}. The face-to-cell distance and the height of pillars are given by δ and h_{p}, respectively. Since an ideal Cassie-Baxter state is assumed, the apparent contact area and the boundary area of computational cells are considered the same and eliminated from the balanced equation. A sketch of the heat balance is shown in Fig. 1 and its formula is given by:

$$k \frac{T_{\mathrm{f}} - T_{\mathrm{c}}}{\delta} = k_{\mathrm{eff}} \frac{T_{\mathrm{s}} - T_{\mathrm{f}}}{h_{\mathrm{p}}}. \tag{21}$$

After mathematical manipulations, the dynamic face temperature T_{f} is obtained as:

$$T_{\mathrm{f}} = \frac{k\, T_{\mathrm{c}} h_{\mathrm{p}} + k_{\mathrm{eff}} T_{\mathrm{s}} \delta}{k h_{\mathrm{p}} + k_{\mathrm{eff}} \delta}. \tag{22}$$

Measurement uncertainty of the drop temperatures

In the experiment performed by Guo et al. [1], thermal images of the droplets by the infrared camera exhibit a deficit, compared to the images by the high-speed camera. As the color bar of the thermal images was set to a range of 23 – 45 °C to exclude the background color corresponding to 50 °C, the portions of the droplet that have a temperature greater than 45 °C are excluded as well. As can be seen by comparing Figs. 6 and 7, the thermal images do not record the lower portion of the droplets during contact. This results from the high temperatures achieved at the bottom during the contact with a hot wall with 60 °C. Hence, the data calculated by the experimental group might not reflect the real temperature of the droplet and could display irregular fluctuations during the contact time. Acknowledging the challenges in capturing the droplet thermal behavior with an infrared camera, validation excludes the data during and after contact. Instead, the focus lies on temperature values prior to the time instant of second contact, specifically during bouncing close to 80 ms. In this range, the droplet heats up during contact for an extended duration and might reach a homogeneous temperature distribution. Hence, its temperature re-enters the measurement limits and also presents the bulk temperature of droplet.

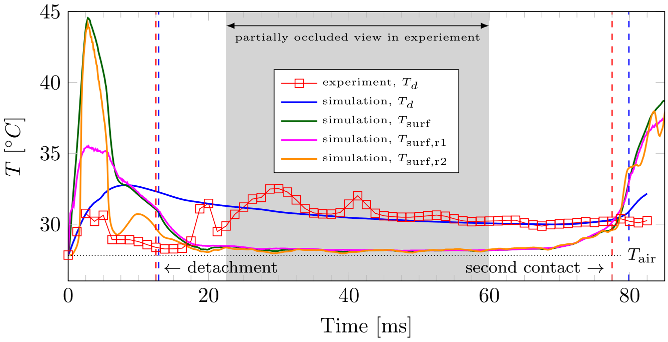

Fig. 17. Comparison of the drop temperature evaluation approaches between experiment and axisymmetric simulation of droplet impact on smooth surface with $d_0 = 2.3\,\mathrm{mm}$, $We = 20$, $T_{\mathrm{d,0}} = 27.8\,°\mathrm{C}$, and $T_{\mathrm{s}} = 60\,°\mathrm{C}$.

For the comparison with the experimental study we consider various drop temperature extraction approaches for the numerical data:

- *Volume-averaged temperature T_d* (Eq. (13))
  The temperature within the liquid phase (phase parameter $C > 0$) is integrated in the 3D-domain.
- *Surface-averaged temperature T_{surf}*
  The temperature is integrated in 3D-domain in the region where the diffuse gas-liquid interface is present ($-0.75 < C < 0.75$).
- *Averaged temperature for the side-view render of the droplet* $T_{\mathrm{surf,r1}}$
  The shape of the droplet is extracted at $C = 0$ and rendered in a lateral perspective using the visualization software package *ParaView*. Subsequently, the obtained surface is color-coded based on its temperature. This rendering process is repeated for each simulation time step, and the resulting images are further post-processed. Specifically, temperature averaging is conducted exclusively on those pixels that convey temperature information.
- *Average of the temperature from the thinned-out render* $T_{\mathrm{surf,r2}}$
  This assessment methodology aims to replicate the post-processing procedures employed in the experimental investigation. The images generated for the estimation of $T_{\mathrm{surf,r1}}$ are subjected to thinning, as outlined in [52], wherein a specified number of pixel layers are removed. This thinning process is implemented to selectively retain the core temperature information and align with the post-processing criteria outlined in the experimental study. The algorithm has been fine-tuned based on the reported post-processing information from the experimental study [1], wherein only the innermost 20% of the imaged droplet was employed for temperature estimation.

Fig. 17 presents the comparison of the results for the considered four approaches. It is evident that the estimations based on surface temperature converge to a consistent level beyond the 20 ms mark, exhibiting overlap up to the second contact point occurring around 80 ms. Nevertheless, this magnitude is lower than the temperature recorded in the experiment by 2-3 °C. Notably, substantial disparities in the evaluation methods emerge during the initial impact of the droplet (before the detachment) and during the final phase (after second contact). In this stage, the visibility of the surface is markedly influenced by the deformation of the droplet, leading to variations in the averaged quantities. The deformation leads to an occurrence of occluded surface areas in the side-view 2D representation, so the predictions rather provide a lower temperature estimations ($T_{\mathrm{surf,r1}}$ and $T_{\mathrm{surf,r2}}$) than the estimations based on the entire 3D surface area (T_{surf}). The evaluations based

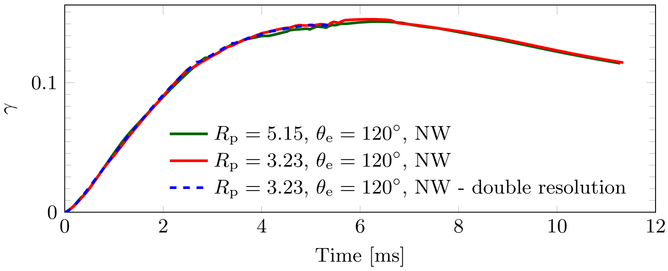

Fig. 18. Bulk cooling effectiveness values of the 3D resolved simulations at $R_p = 3.23$ with $d_0 = 2.3\,\mathrm{mm}$, $We = 20$, NW: Non-wetting.

on thinned-out rendering more accurately capture the temporal evolution of the experiment in the phase preceding droplet detachment. A good alignment between experimental and simulated temperature assessments for the volume-averaged bulk temperature T_d is achieved after 50 ms. This is in agreement with experimental observations that the recorded droplet temperature is intended to represent the bulk temperature just before the second impingement event. At the time instant t =75-80 ms, consistent temperatures are noted across all considered evaluation methods. We hypothesize that the discrepancy between surface-temperature-based estimations from simulation and their experimental counterparts might arise from the intricate transfer function embedded in the experimental IR imaging. Implementing this transfer function accurately with simulation data proves challenging.

Supplementary simulations

Two additional simulations are conducted to confirm the choice of resolution for the 3D resolved simulations, supplementing the presented test cases (see Fig. 18). The first simulation is performed with a surface characterized with $l_{\mathrm{p}} = 0.005d_0$ and $l_{\mathrm{s}} = 0.005d_0, 0.010d_0$. As the grid size and the void ratio ($f_{\mathrm{v}} = 0.85$) is kept consistent throughout the study, this test case results in two different but evenly distributed gap widths in $x-$ and $z-$ directions. The scales of this configuration are closer to the scales of the reference experiment ($l_{\mathrm{p}} \approx 0.003d_0$, $l_{\mathrm{s}} \approx 0.004d_0$). The surface roughness parameter is determined as $R_{\mathrm{p}} = 5.15$. The second simulation represents a more refined version of the case with $R_{\mathrm{p}} = 3.23$, in which only the pin-region resolution close to the structured surface is doubled. Due to the high computational costs this simulation is performed until $t = 5.5$ ms. The results of these simulations are depicted in Fig. 16. As can be seen in the figure, the curves fully overlap with the simulation results carried out at the chosen resolution. A converging wetting behavior of the droplet is observed when the structured surface features becoming smaller.

Appendix A. Supplementary material

Supplementary material related to this article can be found online at https://doi.org/10.1016/j.ijheatmasstransfer.2024.125498.

References

[1] C. Guo, D. Maynes, J. Crockett, D. Zhao, Heat transfer to bouncing droplets on superhydrophobic surfaces, Int. J. Heat Mass Transf. 137 (2019) 857–867, https://doi.org/10.1016/j.ijheatmasstransfer.2019.03.103.

[2] G. Liang, I. Mudawar, Review of drop impact on heated walls, Int. J. Heat Mass Transf. 106 (2017) 103–126, https://doi.org/10.1016/j.ijheatmasstransfer.2016.10.031.

[3] S. Misyura, G. Kuznetsov, D. Feoktistov, R. Volkov, V. Morozov, E. Orlova, The influence of the surface microtexture on wettability properties and drop evaporation, Surf. Coat. Technol. 375 (2019) 458–467, https://doi.org/10.1016/j.surfcoat.2019.07.058.

[4] M. Börnhorst, O. Deutschmann, Single droplet impingement of urea water solution on a heated substrate, Int. J. Heat Fluid Flow 69 (2018) 55–61, https://doi.org/10.1016/j.ijheatfluidflow.2017.10.007.

[5] M. Wörner, N. Samkhaniani, X. Cai, Y. Wu, A. Majumdar, H. Marschall, B. Frohnapfel, O. Deutschmann, Spreading and rebound dynamics of sub-millimetre urea-water-solution droplets impinging on substrates of varying wettability, Appl. Math. Model. 95 (2021) 53–73, https://doi.org/10.1016/j.apm.2021.01.038.

[6] J. Dörnhöfer, M. Börnhorst, C. Ates, N. Samkhaniani, J. Pfeil, M. Wörner, R. Koch, H.-J. Bauer, O. Deutschmann, B. Frohnapfel, et al., A holistic view on urea injection for nox emission control: impingement, re-atomization, and deposit formation, Emission Contr. Sci. Technol. 6 (2) (2020) 228–243, https://doi.org/10.1007/s40825-019-00151-0.

[7] W.-L. Cheng, W.-W. Zhang, H. Chen, L. Hu, Spray cooling and flash evaporation cooling: the current development and application, Renew. Sustain. Energy Rev. 55 (2016) 614–628, https://doi.org/10.1016/j.rser.2015.11.014.

[8] R. Xu, G. Wang, P. Jiang, Spray cooling on enhanced surfaces: a review of the progress and mechanisms, J. Electron. Packag. 144 (1) (2021) 010802, https://doi.org/10.1115/1.4050046.

[9] B. Li, J. Bai, J. He, C. Ding, X. Dai, W. Ci, T. Zhu, R. Liao, Y. Yuan, A review on superhydrophobic surface with anti-icing properties in overhead transmission lines, Coatings 13 (2) (2023), https://doi.org/10.3390/coatings13020301.

[10] I.S. Bayer, Superhydrophobic coatings from ecofriendly materials and processes: a review, Adv. Mater. Interfaces 7 (13) (2020) 2000095, https://doi.org/10.1002/admi.202000095.

[11] F. Wang, C. Liang, X. Zhang, Research of anti-frosting technology in refrigeration and air conditioning fields: a review, Renew. Sustain. Energy Rev. 81 (2018) 707–722, https://doi.org/10.1016/j.rser.2017.08.046.

[12] O. Volodin, N. Pecherkin, A. Pavlenko, N. Zubkov, Surface microstructures for boiling and evaporation enhancement in falling films of low-viscosity fluids, Int. J. Heat Mass Transf. 155 (2020) 119722, https://doi.org/10.1016/j.ijheatmasstransfer.2020.119722.

[13] R. Rioboo, C. Tropea, M. Marengo, Outcomes from a drop impact on solid surfaces, At. Sprays 11 (2) (2001) 155–166, https://doi.org/10.1615/AtomizSpr.v11.i2.40.

[14] R.K. Singh, P.D. Hodgson, N. Sen, S. Das, Effect of surface roughness on hydrodynamic characteristics of an impinging droplet, Langmuir 37 (10) (2021) 3038–3048, https://doi.org/10.1021/acs.langmuir.0c03193.

[15] R.N. Wenzel, Resistance of solid surfaces to wetting by water, Ind. Eng. Chem. 28 (8) (1936) 988–994, https://doi.org/10.1021/ie50320a024.

[16] S. Wang, L. Jiang, Definition of superhydrophobic states, Adv. Mater. 19 (21) (2007) 3423–3424, https://doi.org/10.1002/adma.200700934.

[17] A.B.D. Cassie, S. Baxter, Wettability of porous surfaces, Trans. Faraday Soc. 40 (1944) 546–551, https://doi.org/10.1039/TF9444000546.

[18] X. Huang, I. Gates, Apparent contact angle around the periphery of a liquid drop on roughened surfaces, Sci. Rep. 10 (1) (2020) 1–11, https://doi.org/10.1038/s41598-020-65122-w.

[19] D. Sivakumar, K. Katagiri, T. Sato, H. Nishiyama, Spreading behavior of an impacting drop on a structured rough surface, Phys. Fluids 17 (10) (2005) 100608, https://doi.org/10.1063/1.2033627.

[20] G. Liang, Y. Chen, L. Chen, S. Shen, Maximum spreading for liquid drop impacting on solid surface, Ind. Eng. Chem. Res. 58 (23) (2019) 10053–10063, https://doi.org/10.1021/acs.iecr.9b02014.

[21] R. Kannan, D. Sivakumar, Drop impact process on a hydrophobic grooved surface, Colloids Surf. A, Physicochem. Eng. Asp. 317 (1–3) (2008) 694–704, https://doi.org/10.1016/j.colsurfa.2007.12.005.

[22] V. Fink, X. Cai, A. Stroh, R. Bernard, J. Kriegseis, B. Frohnapfel, H. Marschall, M. Wörner, Drop bouncing by micro-grooves, Int. J. Heat Fluid Flow 70 (2018) 271–278, https://doi.org/10.1016/j.ijheatfluidflow.2018.02.014.

[23] S. Moghtadernejad, C. Lee, M. Jadidi, An introduction of droplet impact dynamics to engineering students, Fluids 5 (3) (2020) 107, https://doi.org/10.3390/fluids5030107.

[24] L. Liu, G. Cai, P.A. Tsai, Drop impact on heated nanostructures, Langmuir 36 (34) (2020) 10051–10060, https://doi.org/10.1021/acs.langmuir.0c01151.

[25] S. Ogata, R. Nakanishi, Effect of surface textures and wettability on droplet impact on a heated surface, Processes 9 (2) (2021) 350, https://doi.org/10.3390/pr9020350.

[26] J. Li, P.B. Weisensee, Low Weber number droplet impact on heated hydrophobic surfaces, Exp. Therm. Fluid Sci. 130 (2022) 110503, https://doi.org/10.1016/j.expthermflusci.2021.110503.

[27] I.V. Roisman, Fast forced liquid film spreading on a substrate: flow, heat transfer and phase transition, J. Fluid Mech. 656 (2010) 189–204, https://doi.org/10.1017/S0022112010001126.

[28] N. Samkhaniani, A. Stroh, M. Holzinger, H. Marschall, B. Frohnapfel, M. Wörner, Bouncing drop impingement on heated hydrophobic surfaces, Int. J. Heat Mass Transf. 180 (2021) 121777, https://doi.org/10.1016/j.ijheatmasstransfer.2021.121777.

[29] N. Samkhaniani, H. Marschall, A. Stroh, B. Frohnapfel, M. Wörner, Numerical simulation of drop impingement and bouncing on a heated hydrophobic surface, J. Phys. Conf. Ser. 2116 (2021) 012073, https://doi.org/10.1088/1742-6596/2116/1/012073.

[30] G. Strotos, M. Gavaises, A. Theodorakakos, G. Bergeles, Numerical investigation of the cooling effectiveness of a droplet impinging on a heated surface, Int. J. Heat Mass Transf. 51 (19-20) (2008) 4728–4742, https://doi.org/10.1016/j.ijheatmasstransfer.2008.02.036.

[31] G. Strotos, G. Aleksis, M. Gavaises, K.-S. Nikas, N. Nikolopoulos, A. Theodorakakos, Non-dimensionalisation parameters for predicting the cooling effectiveness of droplets impinging on moderate temperature solid surfaces, Int. J. Therm. Sci. 50 (5) (2011) 698–711, https://doi.org/10.1016/j.ijthermalsci.2010.11.021.

[32] J.H. Moon, M. Cho, S.H. Lee, Dynamic wetting and heat transfer characteristics of a liquid droplet impinging on heated textured surfaces, Int. J. Heat Mass Transf. 97 (2016) 308–317, https://doi.org/10.1016/j.ijheatmasstransfer.2016.02.041.

[33] M. Bagheri, B. Stumpf, I.V. Roisman, A. Dadvand, M. Wörner, H. Marschall, A unified finite volume framework for phase-field simulations of an arbitrary number of fluid phases, Can. J. Chem. Eng. 100 (9) (2022) 2291–2308, https://doi.org/10.1002/cjce.24510.

[34] F. Jamshidi, H. Heimel, M. Hasert, X. Cai, O. Deutschmann, H. Marschall, M. Wörner, On suitability of phase-field and algebraic volume-of-fluid OpenFOAM® solvers for gas–liquid microfluidic applications, Comput. Phys. Commun. 236 (2019) 72–85, https://doi.org/10.1016/j.cpc.2018.10.015.

[35] P. Yue, C. Zhou, J.J. Feng, Sharp-interface limit of the Cahn–Hilliard model for moving contact lines, J. Fluid Mech. 645 (2010) 279–294, https://doi.org/10.1017/S0022112009992679.

[36] W. Villanueva, G. Amberg, Some generic capillary-driven flows, Int. J. Multiph. Flow 32 (9) (2006) 1072–1086, https://doi.org/10.1016/j.ijmultiphaseflow.2006.05.003.

[37] C.-O. Ng, C. Wang, Temperature jump coefficient for superhydrophobic surfaces, J. Heat Transf. 136 (6) (2014) 064501, https://doi.org/10.1115/1.4026499.

[38] X. Cai, H. Marschall, M. Wörner, O. Deutschmann, Numerical simulation of wetting phenomena with a phase-field method using openfoam®, Chem. Eng. Technol. 38 (11) (2015) 1985–1992, https://doi.org/10.1002/ceat.201500089.

[39] X. Cai, M. Wörner, H. Marschall, O. Deutschmann, Numerical study on the wettability dependent interaction of a rising bubble with a periodic open cellular structure, Catal. Today 273 (2016) 151–160, https://doi.org/10.1016/j.cattod.2016.03.053.

[40] X. Cai, M. Wörner, H. Marschall, O. Deutschmann, Cfd simulation of liquid back suction and gas bubble formation in a circular tube with sudden or gradual expansion, Emission Contr. Sci. Technol. 3 (2017) 289–301, https://doi.org/10.1007/s40825-017-0073-3.

[41] X. Jiang, E. Xu, G. Wu, H.Z. Li, Drop impact on superhydrophobic surface with protrusions, Chem. Eng. Sci. 212 (2020) 115351, https://doi.org/10.1016/j.ces.2019.115351.

[42] E. Gelissen, C. van der Geld, M. Baltussen, J. Kuerten, Modeling of droplet impact on a heated solid surface with a diffuse interface model, Int. J. Multiph. Flow 123 (2020) 103173, https://doi.org/10.1016/j.ijmultiphaseflow.2019.103173.

[43] Y. Ma, Z. Zhou, F. Zhang, Y. Cheng, J. Xu, Numerical investigation of impacting heat transfer of binary droplets on superhydrophobic substrates, Int. J. Therm. Sci. 192 (2023) 108381, https://doi.org/10.1016/j.ijthermalsci.2023.108381.

[44] A.P. Bowles, C.D.F. Honig, W.A. Ducker, No-slip boundary condition for weak solid-liquid interactions, J. Phys. Chem. C 115 (17) (2011) 8613–8621, https://doi.org/10.1021/jp1106108.

[45] A.M.P. Boelens, J.J. de Pablo, Generalised Navier boundary condition for a volume of fluid approach using a finite-volume method, Phys. Fluids 31 (2) (2018) 021203, https://doi.org/10.1063/1.5055036.

[46] A. Chandramohan, J.A. Weibel, S.V. Garimella, Spatiotemporal infrared measurement of interface temperatures during water droplet evaporation on a nonwetting substrate, Appl. Phys. Lett. 110 (4) (2017).

[47] H. Li, I. Roisman, C. Tropea, Influence of solidification on the impact of supercooled water drops onto cold surfaces, Exp. Fluids 56 (2015) 1–13.

[48] K.L. Wilke, Y. Song, Z. Lu, E.N. Wang, Enhanced Laplace pressures for functional surfaces: wicking, switchability, and selectivity, Adv. Mater. Interfaces 10 (4) (2023) 2201967, https://doi.org/10.1002/admi.202201967.

[49] S. Herbert, T. Gambaryan-Roisman, P. Stephan, Influence of the governing dimensionless parameters on heat transfer during single drop impingement onto a hot wall, Colloids Surf. A, Physicochem. Eng. Asp. 432 (2013) 57–63, https://doi.org/10.1016/j.colsurfa.2013.05.014.

[50] E. Teodori, P. Pontes, A. Moita, A. Moreira, Thermographic analysis of interfacial heat transfer mechanisms on droplet/wall interactions with high temporal and spatial resolution, Exp. Therm. Fluid Sci. 96 (2018) 284–294, https://doi.org/10.1016/j.expthermflusci.2018.03.013.

[51] W. Qi, P.B. Weisensee, Dynamic wetting and heat transfer during droplet impact on bi-phobic wettability-patterned surfaces, Phys. Fluids 32 (6) (2020) 067110, https://doi.org/10.1063/5.0010877.

[52] L. Lam, S.-W. Lee, C.Y. Suen, Thinning methodologies-a comprehensive survey, IEEE Trans. Pattern Anal. Mach. Intell. 14 (09) (1992) 869–885, https://doi.org/10.1109/34.161346.